MOF-derived $NiCo_2S_4$ and carbon hybrid hollow spheres compactly concatenated by electrospun carbon nanofibers as self-standing electrodes for aqueous alkaline Zn batteries

Jiaqi Yu,[a] Daoping Cai,*[b] Junhui Si,[a] Hongbing Zhan,[b] and Qianting Wang *[a,c]

[a] School of Materials Science and Engineering, Fujian University of Technology, Fuzhou 350118, China.

[b] College of Materials Science and Engineering, Fuzhou University, Fuzhou 350108, China.

[c] Sanming University, Sanming 365004, China.

*Corresponding authors: Daoping Cai and Qianting Wang.

E–mail addresses: dpcai@fzu.edu.cn and wqt@fjut.edu.cn.

Abstract

The development of high-performance cathode materials is of great importance for aqueous alkaline Zn batteries (AZBs) but also remains great challenging. Herein, we demonstrate the rational design and synthesis of $NiCo_2S_4$ nanoparticles and hollow carbon hybrid spheres compactly concatenated by carbon fibers (denoted as $NiCo_2S_4$/HCS@CFs) through an innovative combination of metal–organic framework (MOF)-derived strategy and electrospinning technique. The as-synthesized $NiCo_2S_4$/HCS@CFs film is flexible, lightweight, and free of any polymer binders, which offers multilevel advantages including high electrical conductivity, abundant electroactive sites, fast ion diffusion, facile electrolyte permeability and robust structure stability. When evaluated as self-standing cathode electrodes, as expect, the resulting $NiCo_2S_4$/HCS@CFs//Zn batteries exhibit an extreme high capacity of 343.1 mAh g^{-1} at a current density of 3.8 A g^{-1} (based on the $NiCo_2S_4$ active material), as well as superior rate performance and decent cycling performance. Moreover, corresponding quasi-solid-state batteries are also fabricated to confirm the potential for practical applications. Remarkably, the energy densities of $NiCo_2S_4$/HCS@CFs//Zn batteries are 563.2 Wh kg^{-1} and 49.1 mWh cm^{-3} (liquid) and 504.1 Wh kg^{-1} and 43.9 mWh cm^{-3} (quasi-solid-state). What's more, density functional theory (DFT) calculations reveal the $NiCo_2S_4$/HCS@CFs has strong adsorption ability for OH^- ions. This work not only highlights the importance of developing advanced flexible and lightweight cathode electrodes for aqueous AZBs, but also provides some insights into electrode designs for other energy storage devices.

Keywords: Metal-organic frameworks; Hollow structures; Electrospinning; Cathode materials; Aqueous alkaline Zn batteries.

1. Introduction

Compared with commercial lithium-ion batteries using flammable and toxic organic electrolytes, aqueous rechargeable batteries have aroused intensive attentions in terms of their intrinsic safety, low cost and environmental benignity.[1-3] Besides, the ionic conductivity of aqueous electrolyte (~1 S cm^{-1}) is much higher than that of the organic electrolyte.[4,5] Among them, aqueous alkaline Zn batteries (AZBs) have drawn particular research interests owing to the high theoretical capacity of Zn anode (820 mAh g^{-1} and 5854 mAh cm^{-3}), low redox potential (−0.76 V *vs* standard hydrogen electrode), good stability in water, high natural abundance and nontoxicity.[6-9] Currently, the core for developing high-performance aqueous AZBs is to explore appropriate cathode materials. Compared to other kinds of cathode materials, Ni/Co-based compounds possess high theoretical capacity, high operating voltage and large energy density, which hold great promise for aqueous AZBs.[10-14] However, the low electrical conductivity and low utilization of the Ni/Co-based cathode materials result in unsatisfactory performance.

In recent years, considerable efforts have been made to improving the performance of Ni/Co-based cathode materials for aqueous AZBs. So far, a large number of advanced cathode materials, such as $Ni(OH)_2$, Co_3O_4, NiO, Ni-Co LDH, $NiCo_2O_4$, and $NiMoO_4$, have been reported.[15-24] For example, Lu and coworkers demonstrated the performance of $NiCo_2O_4$ nanosheets was greatly enhanced by oxygen-vacancy and surface phosphate ions modulation.[19] Chen and coworkers reported the F doping Ni/Co hydroxides/oxides/phosphides as the cathode materials and the effect of anion substitution was deeply investigated.[23] In spite of these progresses, the utilization of heavy current collectors and relatively low mass loading of active materials will seriously decrease the overall capacity based on the entire cathode, which can not meet the demands for practical applications.[25,26] Since first reported by Formhals, electrospinning has been regarded as an effective and scalable technique to synthesize self-standing film electrodes.[27-35] The electroactive materials have strong connection with the one dimensional (1D) electrospun carbon fibers,

which is beneficial for fast electron transportation. Inspired by this, in our previous work, we reported the synthesis of small $NiCo_2S_4$ nanoparticles coupled with carbon nanofibers by electrospinning technique for aqueous AZBs, which exhibited a high discharge capacity of 203 mAh g^{-1} at the current density of 2 mA cm^{-2} based on the entire cathode.[36] Therefore, it would be very important to synthesize self-standing Ni/Co-based cathodes for aqueous AZBs through electrospinning method.

Metal-organic frameworks (MOFs) are a novel family of functional materials consisted of metal ions coordinated to organic ligands.[37,38] Recently, MOFs have been constantly adopted as ideal precursors or templates to prepare advanced electrode materials for various energy storage applications, such as supercapacitors, lithium-ion batteries, sodium-ion batteries and lithium-sulfur batteries.[39-43] It is noteworthy that MOFs-derived materials usually possess favorable porous and hollow structures, which is advantages for exposing more electroactive sites and shortening electron/ion transport pathway. For example, porous and hollow $ZnO/ZnFe_2O_4/C$ octahedra derived from Fe-modified MOF-5 delivered a high reversible capacity of 988 mAh g^{-1} for lithium-ion batteries.[41] Hollow Co_4N and carbon nanocages derived from ZIF-8@ZIF-67 structure displayed a large reversible capacity of 1242 mAh g^{-1} at 0.1 C for lithium-sulfur batteries.[43] Nevertheless, the MOFs-derived materials have rarely been reported in the field of aqueous AZBs so far. Based on the above considerations, it should be of great meaningful to combine MOFs-derived strategy and electrospinning technique to construct advanced cathode electrodes for aqueous AZBs.

In this work, we reported the rational design and synthesis of MOF-derived $NiCo_2S_4$ nanoparticles and hollow carbon hybrid spheres compactly concatenated by electrospun carbon fibers (denoted as $NiCo_2S_4$/HCS@CFs) as self-standing cathode electrodes for aqueous AZBs. The $NiCo_2S_4$/HCSs@CFs film is flexible, lightweight and binder-free. Compared with Ni/Co-based oxide and hydroxide counterparts, bimetallic $NiCo_2S_4$ is more appealing as a cathode material by virtue of the higher electrical conductivity and better electrochemical activity.[36,44-46] The as-synthesized $NiCo_2S_4$/HCSs@CFs film cathode has many apparent advantages: (1) The hollow and

porous structure can supply more reaction active sites and facilitate the ion diffusion; (2) The $NiCo_2S_4$ nanoparticles are tightly coupled with the carbon to enhance the electrical conductivity; (3) The electrospun $NiCo_2S_4$/HCSs@CFs are interwoven with each other, which can enhance the structural stability; (4) The free-standing $NiCo_2S_4$/HCSs@CFs film as cathode electrode is free of any binder and conductive carbon. As a result, the self-standing $NiCo_2S_4$/HCS@CFs cathode manifests remarkable electrochemical performance in terms of high discharge capacity (343.1 mAh g^{-1} at 3.8 A g^{-1}), as well as superior rate capability and decent cycling performance. More importantly, by using polyvinyl alcohol (PVA)-KOH gel as electrolyte, quasi-solid-state $NiCo_2S_4$/HCS@CFs//Zn batteries are also assembled and exhibit a high capacity of 165.6 mAh g^{-1} at 1 A g^{-1}, revealing the potential for practical applications.

2. Results and discussion

The synthetic process for the self-standing $NiCo_2S_4$/HCS@CFs film is schematically shown in **Fig. 1**. Firstly, bimetallic NiCo-MOF spheres with a Ni/Co molar ratio of 1:2 are synthesized via a solvothermal method.[46] Secondly, the NiCo-MOF spheres are electrospun with polyacrylonitrile (PAN) to form necklace-like NiCo-MOF@PAN fibers (denoted as NiCo-MOF@PFs). After carbonization in N_2 atmosphere, the NiCo-MOF@PFs is converted to bimetallic NiCo nanoparticles embedded in hollow carbon spheres@carbon fibers (denoted as NiCo/HCS@CFs). At last, the self-standing $NiCo_2S_4$/HCS@CFs film is obtained through a facile hydrothermal sulfidation treatment of the NiCo/HCS@CFs.

The morphological and and structural characteristics of the products were first characterized by scanning electron microscopy (SEM). As shown in **Fig. 2a** and **S1a**, the solid NiCo-MOF spheres show smooth surface with a uniform diameter of 800 nm to 1.2 μm. The X-ray diffraction (XRD) pattern indicates the NiCo-MOF spheres are amorphous (**Fig. S1b**), which agrees well with previous literature.[46] The Fourier transform infrared (FTIR) spectra also confirm the formation of the NiCo-MOF spheres (**Fig. S1c**).[40] Subsequently, the mixture of NiCo-MOF spheres and PAN in dimethyl formamide (DMF) solution is electrospun into fibers (**Fig. S2**). As shown in

Fig. 2b and **c**, the NiCo-MOF spheres are compactly concatenated by PAN to form necklace-like NiCo-MOF@PFs. After carbonization at a high temperature of 750 ℃, the colour of the NiCo-MOF@PFs film turns from light pink to black. As seen in **Fig. S3**, the NiCo/HCS@CFs maintains the fibrous morphology without obvious structure damage. Interestingly, the NiCo-MOF derived NiCo/HCS spheres present unique hollow interior. Energy dispersive spectroscopy (EDS) analysis confirms the Ni/Co molar ratio in NiCo/HCS@CFs is about 1:2 (**Fig. S4**). The average diameter of the NiCo/HCS@CFs is around 1.5 μm while the length can reach up to tens of micrometers. These electrospun fibers with large aspect ratio are interwoven with each other, which is beneficial for fast ions/ electrons transportation and robust structural stability.[28,29]

Fig. 2d and **e** show the SEM images of the $NiCo_2S_4$/HCS@CFs at low and high magnifications. The morphology and structure are almost unchanged after the hydrothermal sulfidation reaction. Notably, the $NiCo_2S_4$/HCS@CFs film shows excellent flexibility, which can be well recovered to its original shape after bending and rolling **(Fig. S5)**. From the side view (**Fig. 2f**), the thickness of the $NiCo_2S_4$/HCS@CFs film is about 113.8 μm. Element mapping indicates the uniform distribution of Ni, Co, S, C and N elements, and the atomic ratio of Ni, Co, S elements is around 1: 2: 4 (**Fig. 2g** and **Fig. S6**). The detailed structural feature of the $NiCo_2S_4$/HCS@CFs was further investigated by transmission electron microscope (TEM). TEM images clearly display the hollow structure of the $NiCo_2S_4$/HCS@CFs (**Fig. 2h** and **i**), which is consistent with SEM observation. Numerous tiny $NiCo_2S_4$ nanoparticles are uniformly distributed on the carbon matrix. In the high resolution TEM (HRTEM) image, it can be seen the $NiCo_2S_4$ nanoparticles have strong coupling effect with the carbon. The lattice fringes of 0.34 nm could be ascribed to the (002) plane of graphite carbon, while the lattice spacings of 0.23 nm can be assigned to the (400) plane of $NiCo_2S_4$ (**Fig. 2j**). For comparison, the $NiCo_2S_4$@CFs film is also synthesized via the conventional electrospinning method**.** Typically, cobalt acetate ($Co(Ac)_2$) and nickel acetate ($Ni(Ac)_2$) are electrospun with PAN into fibers (**Fig. S7**). After subsequent carbonization and sulfidation treatments, the $NiCo_2S_4$@CFs film is

obtained, as shown in **(Fig. S8)**. Besides, without the addition of Ni and Co sources, pure PFs and corresponding CFs are also synthesized (**Fig. S9**). It is worth to mentioning that the $NiCo_2S_4$/HCS@CFs and $NiCo_2S_4$@CFs film are lightweight (1.87 and 1.64 mg cm^{-2}) in comparison with the commonly used carbon cloth and nickel foam substrates (**Fig. S10**).

Fig. 3a shows the XRD patterns of the NiCo/HCS@CFs and $NiCo_2S_4$/HCS@CFs. The NiCo/HSC@CFs displays two diffraction peaks at 2θ = 44.5° and 51.8°, which could be indexed to the (111) and (200) planes of metallic Ni and Co or NiCo alloy.[36,43] After sulfidation, the NiCo/HSC@CFs is completely transformed to $NiCo_2S_4$/HCS@CFs. The diffraction peaks at 2θ = 26.8°, 31.5°, 38.2°, 50.3°, 55.1° correspond to the (220), (311), (400), (511) and (440) planes of $NiCo_2S_4$ (JCPDS: 20-0782).[36,47] Similarly, the $NiCo_2S_4$@CFs sample displays the same phase composition (**Fig. S11**). Next, the surface chemical composition of the $NiCo_2S_4$/HCS@CFs was further examined with X-ray photoelectron spectroscopy (XPS). **Fig. 3b** gives its survey spectrum, which further confirms the presence of Ni, Co, S, C and N elements in NiCo/HSC@CFs. For Ni 2p spectrum (**Fig. 3c**), the peaks located at 853.6 and 871.3 eV can be assigned to Ni^{2+}, and peaks at 857.4 and 875.8 eV correspond to Ni^{3+}.[48,49] As for Co 2p spectrum (**Fig. 3d**), the two spin−orbit doublets at 778.9 and 793.9 eV, and 782.4 and 798.5 eV suggest the valence state of Co is also a mixture of +3 and +2.[13,23,50] The XPS spectrum of S 2p is shown in **Fig. 3e**, in which the peaks at 163.5 and 164.7 eV are associated with S $2p_{3/2}$ and S $2p_{1/2}$.[44,45] In **Fig. 3f**, **t**he fitting N 1s spectrum can be resolved into three components, corresponding to pyridinic N (398.9 eV), pyrrolic N (400.3 eV) and graphitic N (401.9 eV), respectively.[30,39] The XPS result indicates the $NiCo_2S_4$/HCS@CFs has a chemical constitution of Ni^{2+}/Ni^{3+} and Co^{2+}/Co^{3+}, which is beneficial for good electrochemical activity.

Fig. 3g and **Fig. S12** give the thermogravimetric analysis (TGA) curves of the $NiCo_2S_4$/HCS@CFs and $NiCo_2S_4$@CFs samples, respectively, which are in accord with previous reports.[36,51,52] Accordingly, the content of $NiCo_2S_4$ in the $NiCo_2S_4$/HCS@CFs and $NiCo_2S_4$@CFs are calculated to be 52.9% and 55.7%,

respectively. In addition, N_2 adsorption-desorption isotherm and pore size distribution curve of the $NiCo_2S_4$/HCS@CFs are shown in **Fig. 3h** and **i**. The specific surface area of the $NiCo_2S_4$/HCS@CFs is as high as 167.0 m^2 g^{-1} and the pore size distribution ranges from 6 to 17 nm in diameter. The large specific surface area and abundant mesopores can supply substantial reaction active sites and facilitate the ion diffusion.[13,24]

To study the electrochemical performance, the aqueous $NiCo_2S_4$/HCS@CFs//Zn battery was assembled with self-standing $NiCo_2S_4$/HCS@CFs film as cathode and a Zn plate as anode, and the schematic illustration is shown in **Fig. 4a**. **Fig. 4b** compares the CV curves of the batteries based on $NiCo_2S_4$/HCS@CFs and $NiCo_2S_4$@CFs cathodes at a scan rate of 5 mV s^{-1}. Evidently, the $NiCo_2S_4$/HCS@CFs cathode shows the larger CV area and redox peak current intensity, indicating improved capacity. Notably, the capacity contribution of the pure CFs could be negligible (**Fig. S13**). The CV curves of $NiCo_2S_4$/HCS@CFs//Zn battery at different scan rates are shown in **Fig. 4c**. With increasing of scan rate, the shape of CV curves is well retained, indicating good rate capability.[15,18] **Fig. 4d** and **Fig. S14** display the typical galvanostatic charge-discharge (GCD) profiles of the $NiCo_2S_4$/HCS@CFs//Zn and $NiCo_2S_4$@CFs//Zn batteries at different current densities ranging from 2 to 10 A g^{-1} (base on entire weight of the cathode). As displayed in **Fig. 4e**, the $NiCo_2S_4$/HCS@CFs cathode yields an incredibly high discharge capacities of 181.7 and 90.3 mAh g^{-1} at current densities of 2 and 10 A g^{-1}, respectively, which are much higher than that of the $NiCo_2S_4$@CFs. Impressively, based on the $NiCo_2S_4$ active material, the specific capacities of the $NiCo_2S_4$/HCS@CFs cathode are calculated to be 343.1, 322.3, 271.3, 211.9 and 170.5 mAh g^{-1} at the current densities of 3.8, 7.6, 11.4, 15.2 and 19.0 A g^{-1}, respectively, which are also higher than that of the $NiCo_2S_4$@CFs cathode (**Fig. 4f** and **Fig. S15**). The high capacity retention as current density increases suggests the excellent rate capability of the $NiCo_2S_4$/HCS@CFs cathode. It is worth to pointing out that the capacity of our work is also higher than other aqueous AZBs previously reported, such as FNCA//Zn,[23] Al-CoNiDH-5%//Zn,[53] CNF@$NiCo_2S_4$//Zn,[36] $NiCo_2O_4$//Zn,[54] NiSe//Zn-KFC,[55] sd-$NiCo_2S_{4-x}$@CC-

1.2 g Na_2S//Zn,[44] CH@NC−LDH@NT//Zn[56] (**Fig. 4i**) and others listed in **Table S1**. Moreover, the volumetric capacities of the $NiCo_2S_4$/HCS@CFs and $NiCo_2S_4$@CFs are as high as 29.9 and 18.9 mAh cm^{-3} at 2 A g^{-1} (**Fig. 4g**), respectively. **Fig. 4h** compares the cycling performance of the $NiCo_2S_4$/HCS@CFs//Zn and $NiCo_2S_4$@CFs//Zn batteries at 5 A g^{-1}. During the cycling process, the Coulombic efficiency of the $NiCo_2S_4$/HCS@CFs//Zn is nearly 100%. Impressively, the $NiCo_2S_4$/HCS@CFs//Zn battery delivers a high capacity retention of 89.2% after 1000 cycles, which also exceeds the value of other aqueous AZBs, such as G-NCGs//Zn (90% after 650 cycles),[57] Al-CoNiDH-5%//Zn (78.1% after 1000 cycles),[53] $NiCo_2O_4$//Zn (63.2% after 1000 cycles),[54] NiSe//Zn-KFC//Zn (63.4% after 1300 cycles),[55] CH@NC−LDH@NT//Zn (71.0% after 800 cycles),[56] and others listed in **Table S1**. Besides, the $NiCo_2S_4$/HCS@CFs cathode after cycling test was examined by SEM, which can maintain the morphology and structure, as shown in **Fig. S16**. While XRD analysis indicates the $NiCo_2S_4$ has transformed to its hydroxide counterparts after cycling (**Fig. S17**).[7,58]

Electrochemical impedance spectroscopy (EIS) measurements were conducted to investigate the resistance of the two cathodes. Obviously, the charge transfer resistance (R_{ct}) of $NiCo_2S_4$/HCS@CFs cathode (2.0 **Ω**) is smaller than that of $NiCo_2S_4$@CFs (10.9 **Ω**), implying the faster charge transfer is achieved in the $NiCo_2S_4$/HCS@CFs cathode (**Fig. 5a**).[59-61] After cycling, the R_{ct} of the $NiCo_2S_4$/HCS@CFs cathode does not change obviously (**Fig. S18**). the The electrochemical reaction kinetics of the $NiCo_2S_4$/HCS@CFs cathode was then studied on the basis of the linear relationship between the peak current (i) and scan rate (v). Herein, the b values for the cathodic and anodic peaks are about 0.55 and 0.57, respectively (**Fig. 5b**), indicating both diffusion- and capacitive-controlled processes are involved.[23,25,44] Besides, the detailed contributions of the two processes can be quantified according to the formula: i (V) = $k_1v + k_2v^{1/2}$. The capacitive contributions at different scan rates of 1, 2, 5 and 10 mV s^{-1} are about 20.4%, 23.7%, 37.3% and 42.9%, respectively (**Fig. 5c**). This result indicates the favorable reaction kinetics in the $NiCo_2S_4$/HCS@CFs cathode. To deeply understand the reason for such excellent

performance, density functional theory (DFT) calculations were performed to investigate the adsorption properties of the OH^- ions on the $NiCo_2S_4$/HCS@CFs. As shown in **Fig. 5d-f**, the theoretical calculation models of carbon, $NiCo_2S_4$ and $NiCo_2S_4$/carbon are constructed. The O atoms of OH^- are well coupled with Ni and Co atoms of the (400) surface of $NiCo_2S_4$. It is calculated that the average adsorption energy of OH^- on (400) surface atoms of $NiCo_2S_4$ is 2.25 eV, which is much higher than that of on carbon (0.80 eV). Furthermore, it is found that the OH^- ions adsorption energy increases to a high value of 2.43 eV after hybrid with carbon (**Fig. 5g**). The DFT calculations confirm the $NiCo_2S_4$/HCS@CFs has high adsorption ability towards the OH^- ions in the electrolyte, thus greatly improving the reaction kinetics.[23,48,58]

To demonstrate the potential for practical applications, the quasi-solid-state battery using $NiCo_2S_4$/HCS@CFs cathode was also fabricated by replacing the liquid electrolyte with quasi-solid-state electrolyte (**Fig. 6a**). **Fig. 6b** compares the CV curves of the $NiCo_2S_4$/HCS@CFs//Zn batteries using quasi-solid-state electrolyte and liquid electrolytes at 1 mV s^{-1}. The integral CV curve area of the quasi-solid-state electrolyte is slightly smaller than that using liquid battery. Remarkably, the maximum capacity is up to 165.6 mAh g^{-1} at 1 A g^{-1} (312.7 mAh g^{-1}, based on the $NiCo_2S_4$ active material) (**Fig. 6c**). The low Coulombic efficiency of the device battery could be owing to some side reactions occurred in gel electrolyte.[6] Compared with the aqueous electrolyte, the R_{ct} resistance of the quasi-solid-state battery slightly increases (**Fig. S19**). The cycling stability of the quasi-solid-state battery is satisfactory, which can maintain 79.0% of the capacity after 200 cycles at 3 A g^{-1} (**Fig. 6d**). As shown in **Fig. 6e**, two quasi-solid-state $NiCo_2S_4$/HCS@CFs//Zn batteries in series can successfully light the red LED light for more than 30 minutes. More importantly, the batteries can continue to work after bending at different angles, showing the great potential for practical application in flexible devices. **Fig. 6f** depicts the Ragone plots comparing the gravimetric energy/power densities of the $NiCo_2S_4$/HCS@CFs//Zn batteries with other reported aqueous AZBs. Impressively, the $NiCo_2S_4$/HCS@CFs//Zn battery exhibits a remarkable energy/power densities of 563.2 Wh kg^{-1}/6.19 kW kg^{-1} (liquid) and 504.1 Wh kg^{-1}/3.04 kW kg^{-1} (quasi-solid-

state) (based on the $NiCo_2S_4$ active material). These values are superior to most of the previously reported batteries, such as G-NCGs//Zn,[57] HD-NiS_2/rGO-5//Zn,[62] Co_3O_4@NiV-LDH NWAs//Zn,[63] Ni/NiO-BCF//Zn,[64] sd-$NiCo_2S_{4-x}$@CC-1.2 g Na_2S//Zn,[44] $CoNi(OH)_2$//NNA@Zn,[65] $NiCo_2O_4$//Zn,[66] and others given in **Table S2**. Additionally, the volumetric energy densities of the $NiCo_2S_4$/HCS@CFs//Zn battery reach to 49.1 mWh cm^{-3} (liquid) and 43.9 mWh cm^{-3} (quasi-solid-state), which are also better than other recent reported aqueous AZBs (**Table S2**).

3. Conclusion

To summarize, we have successfully designed and synthesized the self-standing $NiCo_2S_4$/HCS@CFs film as lightweight, flexible and binder-free cathode electrodes for aqueous AZBs. The synthetic procedure rationally combines the advantages of MOF-derived strategy and electrospinning technique. The $NiCo_2S_4$/HCS units possess favorable hollow interior and are compactly concatenated by the electrospun carbon fibers, thus forming unique necklace-like structures. Benefiting from the apparent structural and compositional advantages, the aqueous AZBs based on $NiCo_2S_4$/HCS@CFs film as cathode exhibits an extreme high capacity of 343.1 mAh g^{-1} at 3.8 A g^{-1} (181.7 mAh g^{-1}, base on entire weight of the cathode), significantly outperforming the $NiCo_2S_4$@CFs counterpart. Even at at a high rate of 19.0 A g^{-1}, the capacity is still as high as 170.5 mAh g^{-1}. When cycling at 5 A g^{-1} for 1000 cycles, about 89.2% capacity retention can be maintained, indicating decent cycling performance. Impressively, the gravimetric/volumetric energy densities of the $NiCo_2S_4$/HCS@CFs//Zn batteries are 563.2 Wh kg^{-1}/49.1 mWh cm^{-3}, respectively.More importantly, the corresponding quasi-solid-state batteries are also fabricated and displayed high capacity (312.7 mAh g^{-1}) and large energy density (504.1 Wh kg^{-1}), indicating the potential applications. In addition, DFT calculations prove the $NiCo_2S_4$/HCS@CFs have strong affinity towards the OH^- ions. The electrochemical results suggest the self-standing $NiCo_2S_4$/HCS@CFs film could hold great promise for aqueous AZBs.

Conflicts of interest

There are no conflicts to declare.

Acknowledgements

This work was supported by Natural Science Foundation of Fujian Province, China (No. 2021J01430167 and 2021J01592), and Open Research Project of Fujian Provincial Engineering Research Center of Die & Mold (No. KF-C19007 and KF-C21005). Program for Innovative Research Team in Science and Technology in Fujian Province University (IRTSTFJ) and Fujian University of Techn ology scientific research fund (No. GY-Z19018).

References

1 Parker, C. N. Chervin, I. R. Pala, M. Machler, M. F. Burz, J. W. Long, D. R. Rolison, *Science*, 2017, **356**, 415-418.

2 C. Yang, J. Chen, X. Ji, T. P. Pollard, X. Lu, C. J. Sun, S. Hou, Q. Liu, C. Liu, T. Qing, Y. Wang, O. Borodin, Y. Ren, K. Xu and C. Wang, *Nature*, 2019, **569**, 245-250.

3 C. Li, L. Wang, J. Zhang, D. Zhang, J. Du, Y. Yao and G. Hong, *Energy Storage Mater.*, 2022, **44**, 104-135.

4 W. Du, E. H. Ang, Y. Yang, Y. Zhang, M. Ye and C. C. Li, *Energy Environ. Sci.*, 2020, **13**, 3330-3360.

5 H. Zhang, Q. Liu, D. Zheng, F. Yang, X. Liu and X. Lu, *Nat. Commun.*, 2021, **12**, 14.

6 H. Li, L. Ma, C. Han, Z. Wang, Z. Liu, Z. Tang and C. Zhi, *Nano Energy*, 2019, **62**, 550-587.

7 Y. Tang, X. Li, H. Lv, D. Xie, W. Wang, C. Zhi and H. Li, *Adv. Energy Mater.*, 2020, **10**, 2000892.

8 X. Li, Y. Tang, H. Lv, W. Wang, F. Mo, G. Liang, C. Zhi and H. Li, *Nanoscale*, 2019, **11**, 17992-18008.

9 Z. Shen, Z. Tang, C. Li, L. Luo, J. Pu, Z. Wen, Y. Liu, Y. Ji, J. Xie, L. Wang, Y. Yao and G. Hong, *Adv. Energy Mater.*, 2021, **11**, 2102055.

10 W. Shang, W. Yu, Y. Liu, R. Li, Y. Dai, C. Cheng, P. Tan and M. Ni, *Energy Storage Mater.*, 2020, **31**, 44-57.

11 W. Zhou, D. Zhu, J. He, J. Li, H. Chen, Y. Chen and D. Chao, *Energy Environ. Sci.*, 2020, **13**, 4157-4167.

12 J. Liu, C. Guan, C. Zhou, Z. Fan, Q. Ke, G. Zhang, C. Liu and J. Wang, *Adv. Mater.*, 2016, **28**, 8732-8739.

13 S. Yang, C. Li, Y. Wang, S. Chen, M. Cui, X. Bai, C. Zhi and H. Li, *Energy Storage Mater.*, 2020, **33**, 230-238.

14 X. Li, Y. Tang, J. Zhu, H. Lv, L. Zhao, W. Wang, C. Zhi and H. Li, *Small*, 2020, **16**, 2001935.

15 T. Chen, Y. Bai, X. Xiao and H. Pang, *Chem. Eng. J.*, 2021, **413**, 127523.

16 M. Gong, Y. Li, H. Zhang, B. Zhang, W. Zhou, J. Feng, H. Wang, Y. Liang, Z. Fan, J. Liu and H. Dai, *Energy Environ. Sci.*, 2014, **7**, 2025-2032.

17 Y. Huang, W. S. Ip, Y. Y. Lau, J. Sun, J. Zeng, N. S. S. Yeung, W. S. Ng, H. Li, Z. Pei, Q. Xue, Y. Wang, J. Yu, H. Hu and C. Zhi, *ACS Nano*, 2017, **11**, 8953-8961.

18 P. Tan, B. Chen, H. Xu, W. Cai, W. He and M. Ni, *Appl. Catal. B*, 2019, **241**, 104-112.

19 Y. Zeng, Z. Lai, Y. Han, H. Zhang, S. Xie and X. Lu, *Adv. Mater.*, 2018, **30**, 1802396.

20 Y. Shen, K. Zhang, F. Yang, Z. Li, Z. Cui, R. Zou, Q. Liu, J. Hu and K. Xu, *Sci. China Mater.*, 2020, **63**, 1205-1215.

21 Z. Tian, Z. Sun, Y. Shao, L. Gao, R. Huang, Y. Shao, R. B. Kaner and J. Sun, *Energy Environ. Sci.*, 2021, **14**, 1602-1611.

22 H. Chen, Z. Shen, Z. Pan, Z. Kou, X. Liu, H. Zhang, Q. Gu, C. Guan and J. Wang, *Adv. Sci.*, 2019, **6**, 1802002.

23 W. Liu, Y. Chen, Y. Wang, Q. Zhao, L. Chen, W. Wei and J. Ma, *Energy Storge Mater.*, 2021, **37**, 336-344.

24 L. Zhou, S. Zeng, D. Zheng, Y. Zeng, F. Wang, W. Xu, J. Liu and X. Lu, *Chem. Eng. J.*, 2020, **400**, 125832.

25 Y. Xie, B. Fei, D. Cai, Q. Chen, Z. Cui, Q. Wang and H. Zhan, *Energy Storage Mater.*, 2020, **31**, 27-35.

26 T. Jin, Q. Han and L. Jiao, *Adv. Mater.*, 2020, **32**, 1806304.

27 Y. Lei, Q. Wang, S. Peng, S. Ramakrishna, D. Zhang and K. Zhou, *Adv. Energy Mater.*, 2020, **10**, 1902115.

28 C. Chen, J. Guan, N. W. Li, Y. Lu, D. Luan, C. H. Zhang, G. Cheng, L. Yu and X. W. Lou, *Adv. Mater.*, 2021, **33**, 2100608.

29 Z. Li, Y. Fang, J. Zhang and X. W. Lou, *Adv. Mater.*, 2018, **30**, 1800525.

30 X. Hu, G. Zhong, J. Li, Y. Liu, J. Yuan, J. Chen, H. Zhan and Z. Wen, *Energy Environ. Sci.*, 2020, **13**, 2431-2440.

31 Z. Li, B. Y. Guan, J. Zhang and X. W. Lou, *Joule*, 2017, **1**, 576-587.

32 D. Wu, W. Zhang, Y. Feng and J. Ma, *J. Mater. Chem. A*, 2020, **8**, 2618-2626.

33 D. Yang, W. Ni, J. Cheng, Z. Wang, T. Wang, Q. Guan, Y. Zhang, H. Wu, X. Li and B. Wang, *Appl. Surf. Sci.*, 2017, **413**, 209-218.

34 W. Ni, J. Cheng, L. Shi, X. Li, B. Wang, Q. Guan, L. Huang, G. Gu and H. Li, *J. Mater. Chem. A*, 2014, **2**, 19122-19130.

35 D. Yang, W. Ni, J. Cheng, Z. Wang, C. Li, Y. Zhang and B. Wang, *Mater. Today Energy*, 2017, **5**, 196-204.

36 Z. Cui, S. Shen, J. Yu, J. Si, D. Cai and Q. Wang, *Chem. Eng. J.*, 2021, **426**, 130068.

37 H. Wu and X. W. Lou, *Sci. Adv.*, 2017, **3**, eaap9252.

38 Y. Bai, C. Liu, Y. Shan, T. Chen, Y. Zhao, C. Yu and H. Pang, *Adv. Energy Mater.*, 2021, **11**, 2100346.

39 L. F. Chen, Y. Lu, L. Yu and X. W. Lou, *Energy Environ. Sci.*, 2017, **10**, 1777-1783.

40 B. Y. Guan, A. Kushima, L. Yu, S. Li, J. Li and X. W. D. Lou, *Adv Mater.*, 2017, **29**. 1605902.

41 F. Zou, X. Hu, Z. Li, L. Qie, C. Hu, R. Zeng, Y. Jiang and Y. Huang, *Adv. Mater.*,

2014, **26**, 6622-6628.

42 Y. Feng, M. Xu, T. He, B. Chen, F. Gu, L. Zu, R. Meng and J. Yang, *Adv. Mater.*, 2021, **33**, 2007262.

43 Z. Sun, S. Vijay, H. H. Heenen, A. Y. S. Eng, W. Tu, Y. Zhao, S. W. Koh, P. Gao, Z. W. Seh, K. Chan and H. Li, *Adv. Energy Mater.*, 2020, **10**, 1904010.

44 C. Han, T. Zhang, J. Li, B. Li and Z. Lin, *Nano Energy*, 2020, **77**, 105165.

45 W. He, S. Wang, Y. Shao, Z. Kong, H. Tu, Y. Wu and X. Hao, *Adv. Energy Mater.*, 2021, **11**, 2003268.

46 M. Yi, C. Zhang, C. Cao, C. Xu, B. Sa, D. Cai and H. Zhan, *Inorg. Chem.*, 2019, **58**, 3916-3924.

47 B. Guo, T. Yang, W. Du, Q. Ma, L.-z. Zhang, S.-J. Bao, X. Li, Y. Chen and M. Xu, *J. Mater. Chem. A*, 2019, **7**, 12276-12282.

48 J. Yang, C. Yu, X. Fan, S. Liang, S. Li, H. Huang, Z. Ling, C. Hao and J. Qiu, *Energy Environ. Sci.,* 2016, **9**, 1299-1307.

49 B. Jin, D. Liu, C. Liu and G. Liu, *RSC Adv.*, 2015, **5**, 84711-84717.

50 R. Li, Y. Pan, B. Luo, J. Zao, Y. Xiao, S. Lei and B. Cheng, *Electrochim. Acta*, 2020, **344**, 135811.

51 Y. Yan, A. Li, C. Lu, T. Zhai, S. Lu, W. Li and W. Zhou, *Chem. Eng. J.*, 2020, **396**, 125316.

52 W. Xin, W. J. Jiang, Y. Lian, H. Li, S. Hong, S. Xu, H. Yan and J. S. Hu, *Chem. Commun.*, 2019, **55**, 6134.

53 . Zhu, Y. Wu, Y. Lu, Y. Sun, Q. Wu, Y. Pang, Z. Shen and H. Chen, *J. Colloid Interface Sci.*, 2021, **587**, 693-702.

54 W. Shang, W. Yu, P. Tan, B. Chen, H. Xu and M. Ni, *J. Power Sources*, 2019, **421**, 6-13.

55 Y. Huang, M. Li, S. Chen, P. Sun, X. Lv, B. Li, L. Fang and X. Sun, *Appl. Surf. Sci.*, 2021, **562**, 150222.

56 Y. Wang, X. Hong, Y. Guo, Y. Zhao, X. Liao, X. Liu, Q. Li, L. He and L. Mai, *Small*, 2020, **16**, e2000293.

57 X. Zhang, J. He, L. Zhou, H. Zhang, Q. Wang, B. Huang, X. Lu, Y. Tong and C.

Wang, *Adv. Funct. Mater.*, 2021, **31**, 2100443.

58 X. Yun, T. Lu, R. Zhou, Z. Lu, J. Li and Y. Zhu, *Chem. Eng. J.*, 2021, **426**, 131328.

59 Y. Wang, L. Zhou, X. Cao, X. Gao and X. Lu, *J. Mater. Chem. A*, 2021, **9**, 26698-26703.

60 Z. Shen, L. Luo, C. Li, J. Pu, J. Xie, L. Wang, Z. Huai, Z. Dai, Y. Yao and G. Hong, *Adv. Energy Mater.*, 2021, **11**, 2100214.

61 M. Chen, J. Chen, W. Zhou, X. Han, Y. Yao and C. P. Wong, *Adv Mater.*, 2021, **33**, 2007559.

62 W. Shi, J. Mao, X. Xu, W. Liu, L. Zhang, X. Cao and X. Lu, *J. Mater. Chem. A*, 2019, **7**, 15654-15661.

63 S. Wang, S. Lai, P. Li, T. Gao, K. Sun, X. Ding, T. Xie, C. Wu, X. Li, Y. Kuang, W. Liu, W. Yang and X. Sun, *J. Power Sources*, 2019, **436**, 226867.

64 L. Jiang, L. Li, S. Luo, H. Xu, L. Xia, H. Wang, X. Liu, Y. Wu and Y. Qing, *Nanoscale*, 2020, **12**, 14651-14660.

65 C. Xu, J. Liao, C. Yang, R. Wang, D. Wu, P. Zou, Z. Lin, B. Li, F. Kang and C.-P. Wong, *Nano Energy*, 2016, **30**, 900-908.

66 H. Zhang, X. Zhang, H. Li, Y. Zhang, Y. Zeng, Y. Tong, P. Zhang and X. Lu, *Green Energy Environ.*, 2018, **3**, 56-62.

Figure captions

Fig. 1. Schematic illustration for synthesizing the self-standing $NiCo_2S_4$/HCS@CFs film.

Fig. 2. SEM images of the (a) NiCo-MOF spheres, (b, c) NiCo-MOF@PFs, (d-f) $NiCo_2S_4$/HCS@CFs, (g) Elemental mapping, (h, i) TEM and (j) HRTEM images of the $NiCo_2S_4$/HCS@CFs.

Fig. 3. (a) XRD patterns of the NiCo/HCS@CFs and $NiCo_2S_4$/HCS@CFs. (b) XPS survey spectrum and high-resolution XPS spectra of the (c) Ni 2p, (d) Co 2p, (e) S 2p, (f) N 1s for the $NiCo_2S_4$/HCS@CFs. (g) TGA curve, (h) N_2 adsorption-desorption isotherm and (i) corresponding pore size distribution of the $NiCo_2S_4$/HSC@CFs.

Fig. 4. (a) Schematic illustration of the aqueous $NiCo_2S_4$/HCS@CFs//Zn battery. (b) CV curves at 5 mV s^{-1} for the $NiCo_2S_4$/HCS@CFs, $NiCo_2S_4$@CFs and CFs cathodes. (c) CV and (d) GCD curves of the $NiCo_2S_4$/HCS@CFs//Zn battery. (e, f) Specific capacities of the $NiCo_2S_4$/HCS@CFs based on the $NiCo_2S_4$ active material and entire weight of the cathode. (g) Volumetic capacities of the $NiCo_2S_4$/HCS@CFs and $NiCo_2S_4$@CFs. (h) Cycling performance. (i) Comparison of the capacities with reported works.

Fig. 5. (a) EIS analyses of the $NiCo_2S_4$/HCS@CFs and $NiCo_2S_4$@CFs cathodes. (b) The plots of log (*i*) against log (*v*) of the $NiCo_2S_4$/HCS@CFs. (c) Corresponding capacitive contribution at various scan rates. Models of the calculation of OH^- adsorption on (d) carbon, (e) $NiCo_2S_4$ and (f) $NiCo_2S_4$/carbon. (g) Adsorption energy of OH^- ions on carbon, $NiCo_2S_4$ and $NiCo_2S_4$/carbon.

Fig. 6. (a) Schematic illustration for the quasi-solid-state $NiCo_2S_4$/HCS@CFs//Zn battery. (b) CV curves of the liquid and quasi-solid-state $NiCo_2S_4$/HCS@CFs//Zn batteries at 1 mV s^{-1}. (c) GCD curves and (d) cycling performance of the quasi-solid-state $NiCo_2S_4$/HCS@CFs//Zn battery. (e) Photos of a LED light lighted by the quasi-solid-state batteries under normal and bending states. (f) Ragone plots of our $NiCo_2S_4$/HCS@CFs//Zn batteries compared to other AZBs.

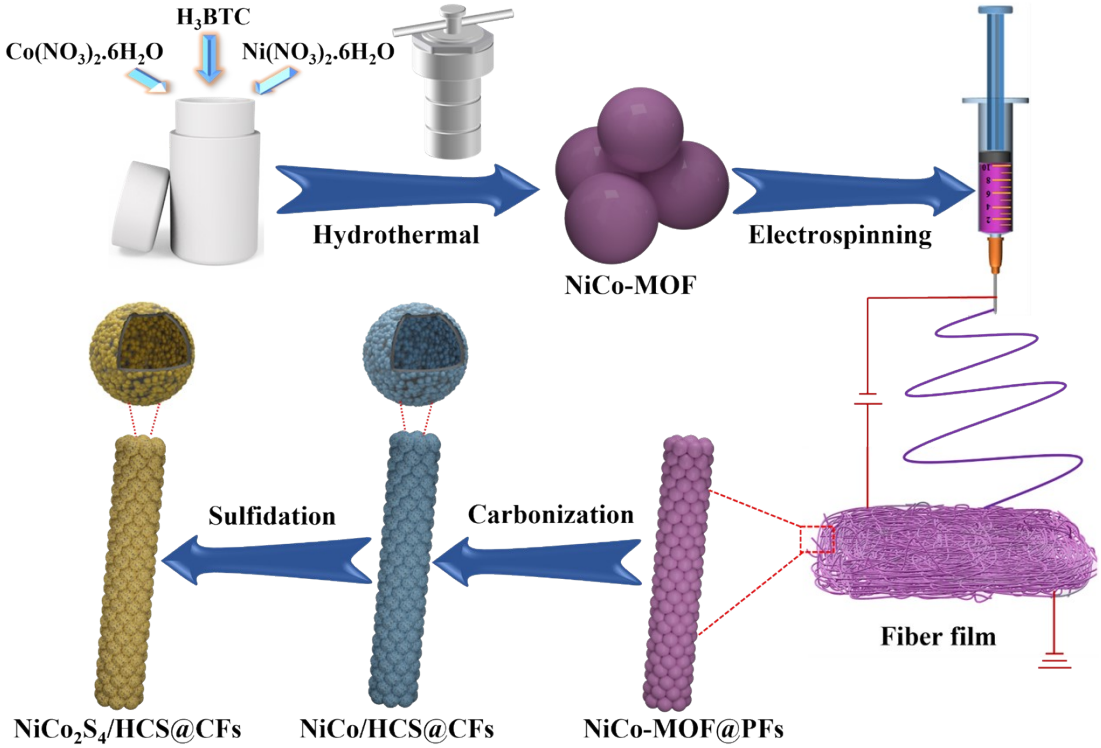

Fig. 1. Schematic illustration for synthesizing the self-standing $NiCo_2S_4$/HCS@CFs film.

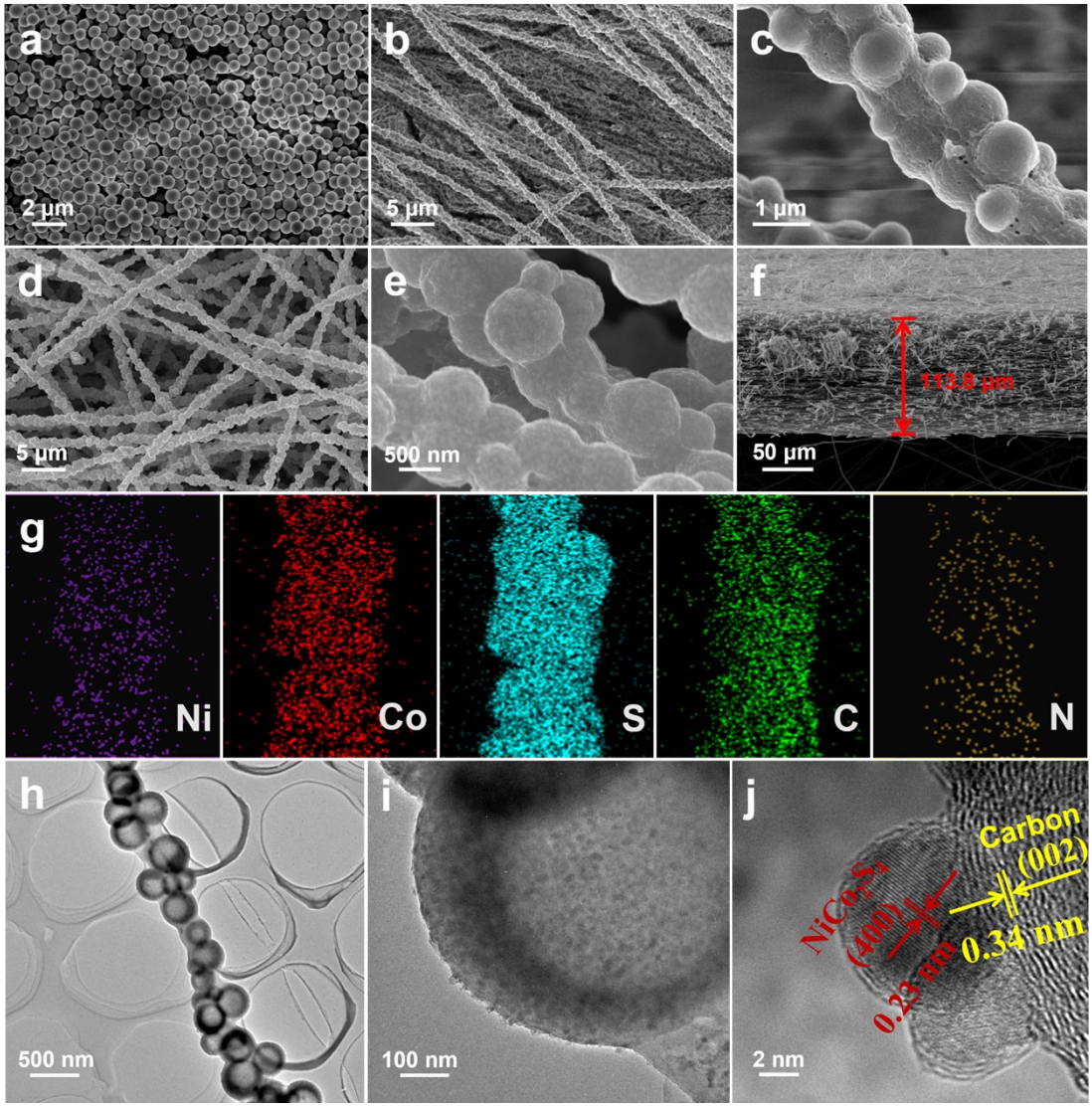

Fig. 2. SEM images of the (a) NiCo-MOF spheres, (b, c) NiCo-MOF@PFs, (d-f) $NiCo_2S_4$/HCS@CFs, (g) Elemental mapping, (h, i) TEM and (j) HRTEM images of the $NiCo_2S_4$/HCS@CFs.

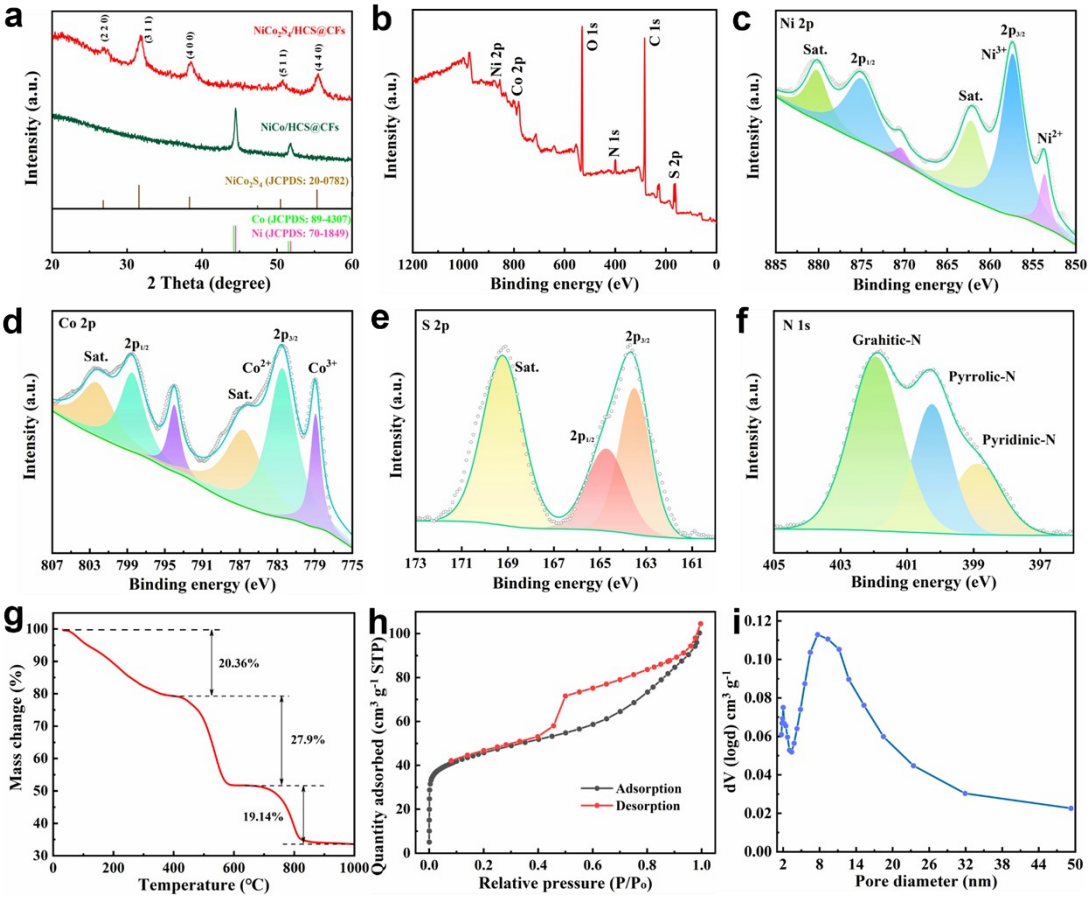

Fig. 3. (a) XRD patterns of the NiCo/HCS@CFs and $NiCo_2S_4$/HCS@CFs. (b) XPS survey spectrum and high-resolution XPS spectra of the (c) Ni 2p, (d) Co 2p, (e) S 2p, (f) N 1s for the $NiCo_2S_4$/HCS@CFs. (g) TGA curve, (h) N_2 adsorption-desorption isotherm and (i) corresponding pore size distribution of the $NiCo_2S_4$/HSC@CFs.

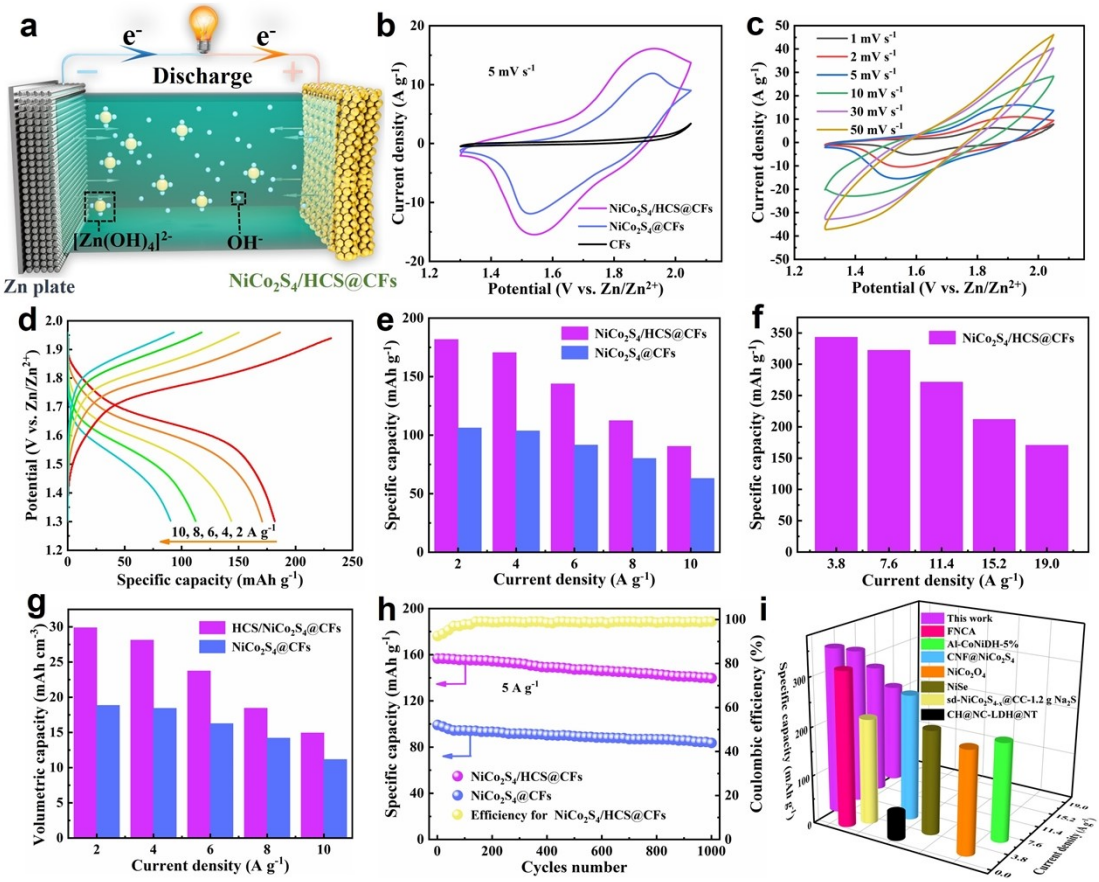

Fig. 4. (a) Schematic illustration of the aqueous $NiCo_2S_4$/HCS@CFs//Zn battery. (b) CV curves at 5 mV s^{-1} for the $NiCo_2S_4$/HCS@CFs, $NiCo_2S_4$@CFs and CFs cathodes. (c) CV and (d) GCD curves of the $NiCo_2S_4$/HCS@CFs//Zn battery. (e, f) Specific capacities of the $NiCo_2S_4$/HCS@CFs based on the $NiCo_2S_4$ active material and entire weight of the cathode. (g) Volumetic capacities of the $NiCo_2S_4$/HCS@CFs and $NiCo_2S_4$@CFs. (h) Cycling performance. (i) Comparison of the capacities with reported works.

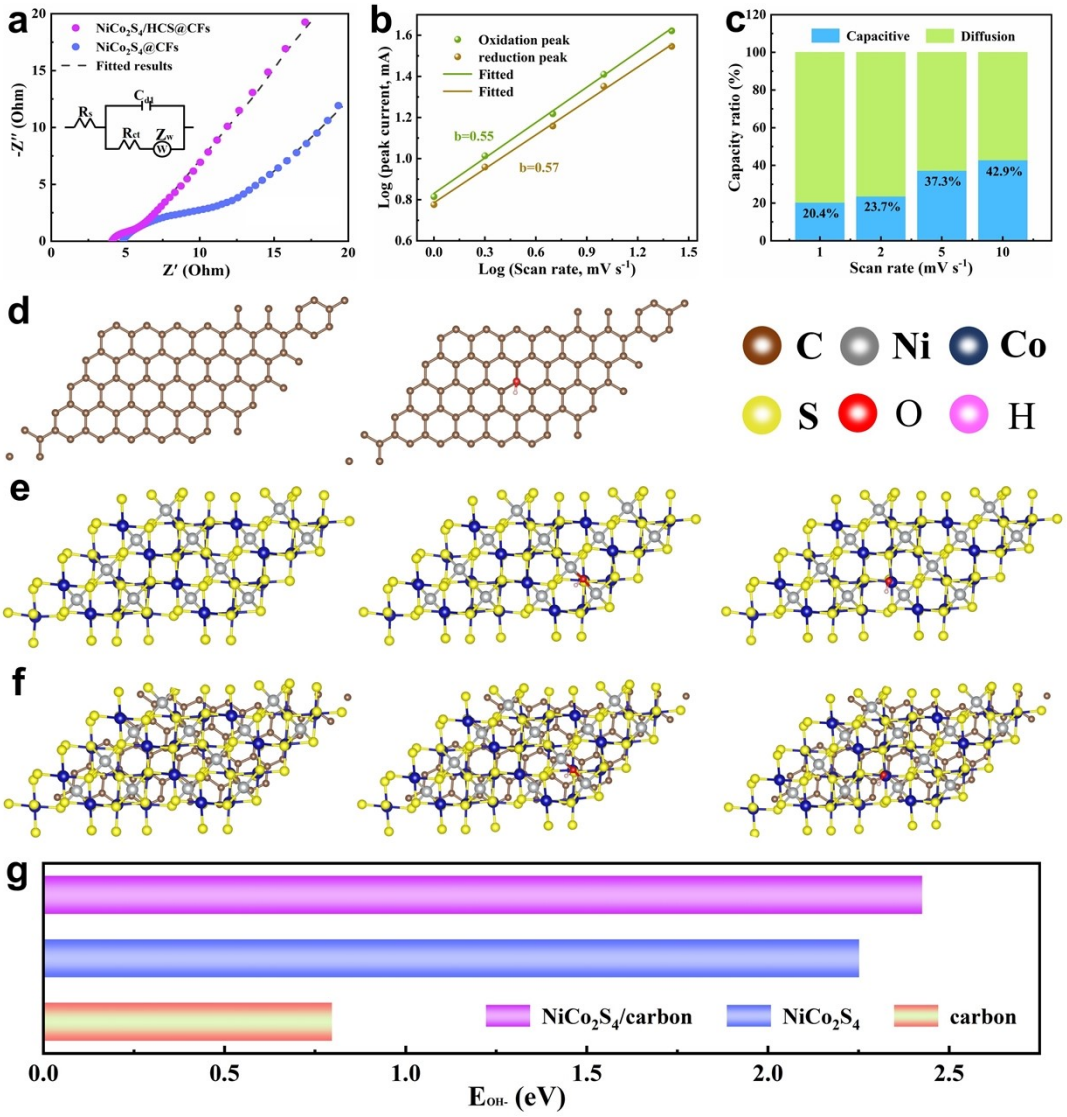

Fig. 5. (a) EIS analyses of the $NiCo_2S_4$/HCS@CFs and $NiCo_2S_4$@CFs cathodes. (b) The plots of log (*i*) against log (*v*) of the $NiCo_2S_4$/HCS@CFs. (c) Corresponding capacitive contribution at various scan rates. Models of the calculation of OH^- adsorption on (d) carbon, (e) $NiCo_2S_4$ and (f) $NiCo_2S_4$/carbon. (g) Adsorption energy of OH^- ions on carbon, $NiCo_2S_4$ and $NiCo_2S_4$/carbon.

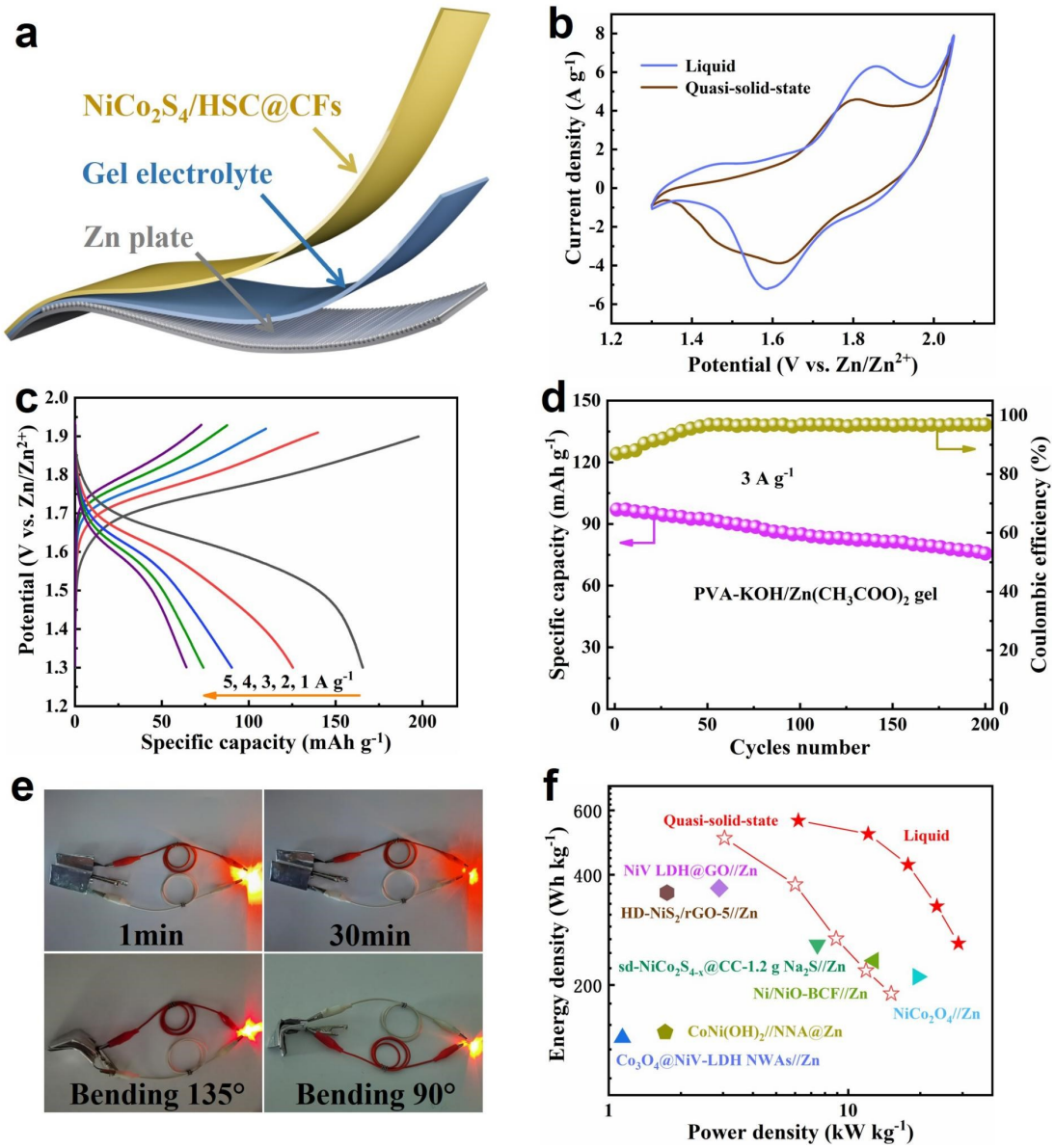

Fig. 6. (a) Schematic illustration for the quasi-solid-state $NiCo_2S_4$/HCS@CFs//Zn battery. (b) CV curves of the liquid and quasi-solid-state $NiCo_2S_4$/HCS@CFs//Zn batteries at 1 mV s^{-1}. (c) GCD curves and (d) cycling performance of the quasi-solid-state $NiCo_2S_4$/HCS@CFs//Zn battery. (e) Photos of a LED light lighted by the quasi-solid-state batteries under normal and bending states. (f) Ragone plots of our $NiCo_2S_4$/HCS@CFs//Zn batteries compared to other AZBs.